



Insight into the function of alkaline earth metal oxides as electron promoters for Au/TiO₂ catalysts used in CO oxidation

Kai Yang^{a,b}, Yongfan Zhang^{a,b}, Yi Li^b, Pan Huang^b, Xun Chen^{a,b}, Wenxin Dai^{a,b,*}, Xianzhi Fu^{a,b}

^a Research Institute of Photocatalysis, State Key Laboratory of Photocatalysis on Energy and Environment, Fuzhou University, Fuzhou 350002, China

^b College of Chemistry, New Campus, Fuzhou University, Fuzhou 350108, China

ARTICLE INFO

Article history:

Received 19 August 2015

Received in revised form

29 September 2015

Accepted 22 October 2015

Available online 27 October 2015

Keywords:

Alkaline earth metal oxide

Au/TiO₂

Electron promoters

Fermi level

DFT calculations

ABSTRACT

Introduction of alkaline earth metal oxide (AEMO) into TiO₂ was found to promote CO oxidation (in the order BaO > SrO > CaO > MgO) over Au nanoparticles supported on TiO₂. From experimental (electron-transfer reaction, CO electrochemical oxidation, CO adsorption and Mott–Schottky plots) and theoretical (density functional theory) calculations, it is proposed that AEMO may act as an electron promoter for CO oxidation, but not as an exclusive structural promoter as widely regarded. Introduction of AEMO raises the Fermi level of the TiO₂ support, resulting in an enhanced electron transfer from the support to the Au sites and promoting activation of CO adsorbed at Au sites. Moreover, the enhanced catalytic activities induced by AEMO depend on the increase in the Fermi level of the support in the order: TiO₂–BaO > TiO₂–SrO > TiO₂–CaO > TiO₂–MgO. This investigation provides a new insight to understand the role of the electron promoters in the thermocatalytic reactions.

© 2015 Elsevier B.V. All rights reserved.

1. Introduction

Over the past three decades, studies on the supported Au catalysts for CO oxidation at low temperatures have resulted in unexpected observations [1,2]. It is generally accepted that the catalytic activities of Au catalysts depend on the nature of Au nanoparticles (NPs) and properties of the supports [3,4]. In this context, the Au deposited typical reducible TiO₂ support is one of the most intensively studied systems [5,6]. Several attempts have been made to improve the catalytic activity of Au/TiO₂ at room temperature, such as doping with nitrogen [7], addition of sulfur [8,9], packing a thin layer of alumina [10], and introducing FeO_x [11], Co₃O₄ [12], and In₂O₃ [13] to the TiO₂ support. These improvements are attributed to the role of the perimeter between Au NPs and supports. Alkaline earth metal oxide (AEMO), usually regarded as structural promoters, can also promote the catalytic activity of Au/TiO₂ for CO oxidation at low temperatures by stronger interactions of low-coordinated Au atoms and Ti cations [14–16]. Some studies [17–19] also indicate that the AEMO incorporated into Au/TiO₂ mainly benefits in stabilizing the Au NPs size, thus promoting CO oxidation. However, to the best of our knowledge, charging

of the supported clusters [20] plays a very important role in promoting the catalytic activity of Au NPs. Previous studies [21–23] have reported that even if the oxide itself had no catalytic activity, charge transport at the oxide–metal interface was one of the major factors accounting for the enhanced activity and selectivity of heterogeneous catalysts. In our previous studies [24–26], we have demonstrated that an increase in the surface electron densities of Au sites induced by electron transfer between the Au NPs and support enhanced the preferential oxidation of CO in the presence of H₂. In fact, Au NPs and supports undergo charge equilibration to drive the energetics of the composites by raising the Fermi level (E_F) to more negative potentials, resulting in a strong electron-donating ability of the composites and an enhanced interfacial charge-transfer efficiency [27,28]. This role of electron transfer or the increase in E_F of the support leads to an increase in the surface electron densities of Au sites and subsequently to the activation of the adsorbed reactant molecules at Au sites (i.e., high electron densities of Au sites lead to a red shift of the C–O vibration of electron back-donation to the CO antibonding orbital) [20].

Based on the aforementioned considerations, we believe that the construction of binary mixed oxides such as AEMO with TiO₂ as a support may also enhance the electron-donating ability of the support. This should promote the catalytic activity of Au NPs for oxidizing CO. To prove this hypothesis, we prepared a series of Au catalysts supported on AEMO (MgO, CaO, SrO and BaO; 10 mol%)-

* Corresponding author. Fax: +86 591 83779083.

E-mail address: daiwenxin@fzu.edu.cn (W. Dai).

modified TiO_2 microspheres with a similar size distribution of Au NPs and tested their catalytic performance for oxidizing CO at room temperature. We herein demonstrated that the intrinsic driving force for the improved catalytic activity of Au/ TiO_2 , activated by the irreducible AEMO, mainly originated from the stronger electronic interactions between Au and AEMO-modified support rather than solely due to the Au NP size effects. Because of a weak change in the valence state in alkaline earth metals, an in-depth understanding of electron promoters was achieved. These findings are also helpful in a comprehensive understanding of CO oxidation on the Au/ TiO_2 system and in designing new Au catalysts with a high catalytic performance.

2. Experimental

2.1. Preparation of catalysts

All the chemicals were of analytical grade and were used as received without further purification. The TiO_2 and TiO_2 -AEMO microsphere supports were prepared by precipitation and hydrothermal procedures. Tetrabutyl titanate (6 mL) was dissolved in ethylene glycol (150 mL). After stirring this solution for 8 h, acetone (300 mL) and deionized water (13.5 mL) were added, and the formed precipitates were filtered, washed with ethanol, and dried at 80 °C. Subsequently, to prepare TiO_2 -AEMO microspheres, the above precursor and a calculated amount of alkaline earth metal nitrate (molar ratio of alkaline earth metal and TiO_2 was 1/10) were dispersed in deionized water (60 mL). The resulting slurry was transferred to a 100 mL Teflon-lined autoclave and placed in an oven for hydrothermal treatment at 180 °C for 10 h. The produced solid precipitates were separated from the solution by centrifugation, the residue was washed several times with distilled water, and finally dried at 80 °C for 12 h in an oven (denoted as TiO_2 , TiO_2 -MgO, TiO_2 -CaO, TiO_2 -SrO, and TiO_2 -BaO based on the used type of alkaline earth metal salt). The actual weight content of Mg, Ca, Sr and Ba elements measured by ICP-MS were 2.57%, 4.32%, 8.13% and 14.06%, respectively.

Au NPs were deposited onto TiO_2 or TiO_2 -AEMO microspheres by a deposition–precipitation process with a theoretical Au loading of 1.0 wt%. Based on the weight of the microspheres, 100 mL suspension including a suitable amount of $\text{HAuCl}_4 \cdot 3\text{H}_2\text{O}$ and the support {the actual weight percentage of Au NPs measured by inductively coupled plasma-mass spectrometry (ICP-MS) over Au/ TiO_2 , Au/ TiO_2 -MgO, Au/ TiO_2 -CaO, Au/ TiO_2 -SrO, and Au/ TiO_2 -BaO were 0.93%, 0.91%, 0.93%, 0.91% and 0.92%, respectively} was poured into a beaker, and the pH value was adjusted to 10.0 by 1.0 M NaOH under vigorous stirring for 12 h at room temperature. This was followed by washing with water, until the AgNO_3 test no longer showed the presence of residual Cl^- , and drying overnight at 80 °C. The obtained products were dispersed in 20 mL deionized water and reduced using a 1.0 M NaBH_4 aqueous solution at room temperature. The products were washed with water and dried at 80 °C. Finally, the Au catalysts were activated at 350 °C for 2 h at a heating rate of 3 °C min⁻¹ in air atmosphere.

2.2. Characterization of catalysts

The X-ray diffraction (XRD) patterns of the catalysts were collected using a Bruker D8 Advance powder X-ray diffractometer using $\text{Cu K}\alpha$ radiation ($\lambda = 0.15418 \text{ nm}$) operated at 40 kV and 40 mA. The actual Au contents of the catalysts were determined by ICP-MS. Particle morphology was investigated using an SU8000 (Hitachi) field-emission scanning electron microscope (SEM). The nanostructure and Au NP size distribution of the synthesized materials were determined by high-resolution transmission electron

microscopy (TEM) and an electron diffraction image using a JEOL JEM-2010 EX with the field emission gun operating at 200 kV. UV-vis diffuse reflectance spectra (UV-vis DRS) of the catalysts were measured using a Varian Cary 5000 UV-vis-NIR spectrophotometer. Raman spectra were recorded on a LabRAM HR UV-NIR microscope (HORIBA Jobin Yvon) at 532 nm using an Ar^+ ion laser. The laser beam intensity and spectrum slit width were 2 mW and 3.5 cm⁻¹, respectively. X-ray photoelectron spectroscopy (XPS) was performed using a Quantum2000 system and the data were collected using an Al $\text{K}\alpha$ X-ray beam (1486.6 eV) operated at 25 W. The C 1s signal of 284.6 eV was used to calibrate the XPS data.

2.3. Measurement of electron transfer reaction

The electron-transfer reactions were monitored by UV-vis spectroscopy. Tetracyanoethylene (TCNE) adsorption and reactions were carried out as follows: A TCNE solution of 1.0 g L⁻¹ was prepared in a 100 mL calibrated flask. Fresh catalyst (0.1 g) and a magnet were placed in a 10 mL flask and pretreated with a N_2 flow for 30 min, and then 1 mL TCNE solution was added. The reaction reached equilibrium after 30 min. For visible light reaction, visible light ($490 \text{ nm} \leq \lambda \leq 760 \text{ nm}$) was introduced into the container. An absorption peak was observed at $\sim 300 \text{ nm}$, indicating that the reaction between Au catalysts and electron acceptor proceeded in the acetonitrile solution, i.e., TCNE was reduced to generate an electron-TCNE complex (TCNE⁻). Therefore, TCNE was used as a probe to better understand the electronic effects on the Au catalytic systems.

2.4. Electrochemical measurements

A three-electrode-compartment electrochemical cell with a platinum wire was used as the counter electrode, and an Ag/AgCl electrode in a saturated KCl solution (+0.24 V vs. normal hydrogen electrode (NHE)) was used as the reference electrode. The catalysts were used as the working electrode, and the electrochemical experiments were performed using an IM6eX electrochemical workstation system (Zahner, Inc., Germany) at room temperature. For CO stripping voltammograms, the solutions were prepared from HClO_4 (0.1 M) and deionized water. First, nitrogen (99.99%) was used to deoxygenate all the solutions, and then 99.99% CO was used to dose CO. The data were recorded at 0.05 V s⁻¹ by first scanning negatively until 0.0 V and then scanning positively until 1.9 V. To obtain the flat band potential of Mott–Schottky plots, the solution was prepared from Na_2SO_4 (0.1 M) and deionized water. Three Mott–Schottky plots were obtained at different frequencies of 0.5 kHz, 1 kHz, and 1.5 kHz. The working electrodes were prepared as follows: First, 10 mg ground sample was added to 5 mL absolute ethanol to prepare the slurry, and then the slurry was injected into a $2.5 \times 1.0 \text{ cm}^2$ indium-tin oxide (ITO) glass with a cell size of $5 \times 5 \text{ mm}^2$ and finally, dried at 100 °C for 300 min.

2.5. CO adsorption of catalysts

Fourier transform infrared spectra (FT-IR) of CO adsorption at room temperature were recorded at atmospheric pressure using an infrared cell reactor (Nicolet Nexus, Model 670) after exposing the samples to CO for 30 min until a steady state was reached. Prior to the admission of CO, an IR background transmission spectrum for sample was recorded. The samples were pressed using a holder fitted with an aluminum foil and placed in a vacuum cell. The samples were pretreated for 2 h at 150 °C.

2.6. Catalytic performances for oxidizing CO

The catalytic oxidation of CO was carried out in a fixed-bed flow reactor at atmospheric pressure using 500 mg of the catalyst at a total flow rate of 100 mL min^{-1} . The catalyst sample with a grain size of 0.2–0.3 mm was placed in a square quartz cell equipped with a cooling water system. The feed stream contained 0.3 vol% CO, 0.3 vol% O₂ and the balance was He. The temperature of the quartz cell was controlled at $\sim 25^\circ\text{C}$ (measured using a thermocouple placed inside the catalyst bed). The outlet stream was analyzed using an online gas chromatograph (GC) system equipped with a thermal conductivity detector (Agilent 7890D, TDX-01). The change in the concentration between the inlet and outlet CO gases was used to calculate the CO conversion (X_{CO}). For the comparison of catalytic activity, turnover frequency (TOF, the turnover number of CO to CO₂ per Au atom per second, s^{-1}) was obtained according to the amount of Au atoms and the space velocity.

The measurements of reaction rate was also performed at atmospheric pressure in a quartz reactor ($1 \times 1 \text{ cm}^2$) with the catalyst powder (10.0 wt%) and quartz sand (90.0 wt%) of 500 mg at a total flow rate of 100 mL min^{-1} with the feed stream of 0.3 vol% CO, 0.3 vol% O₂ and the balanced He. Because a low conversion could ensure the differential nature of the measured rates and avoid more cumbersome interpretation in terms of integral equations. Thus, the samples were diluted with quartz sand, which was not active for CO oxidation under the condition. The values of the conversion were typically limited between 4.0 and 20.0%, where the reaction rate was considered as unchangeable.

X_{CO} , TOF and the reaction rate (r_{CO}) were calculated using the following equations:

$$X_{\text{CO}} = \frac{\{[\text{CO}]_{\text{in}} - [\text{CO}]_{\text{out}}\}}{[\text{CO}]_{\text{in}}}$$

TOF (s^{-1}) = $(N_{\text{CO}} \cdot X_{\text{CO}} \cdot M_{\text{Au}}) / (W_{\text{cat}} \cdot W_{\text{Au}} \cdot D_{\text{Au}})$, where N_{CO} ($\text{mol} \cdot \text{s}^{-1}$) is the molar flow of CO in the feed stream, W_{cat} (g) is the dosage of the catalyst, M_{Au} is molar mass of Au, W_{Au} is the loading amount of Au and D_{Au} is the degree of dispersion about Au nanoparticles. The calculation details of D_{Au} are shown in Supporting information.

On the basis of mass balance, $r_{\text{CO}} = (N_{\text{CO}} \cdot X_{\text{CO}}) / W_{\text{Au}}$, where N_{CO} ($\text{mol} \cdot \text{s}^{-1}$) is the molar flow of CO in the feed stream, W_{Au} (g) is the dosage of gold nanoparticles, r_{CO} ($\text{mol} \cdot \text{g}_{\text{cat}}^{-1} \cdot \text{s}^{-1}$) is the reaction rate of CO oxidation.

2.7. Calculational details

In this study, the projector-augmented wave (PAW) method of density functional theory (DFT) calculations was carried out to investigate the adsorption of different alkaline earth metals (AEMs) on the anatase TiO₂(101) surface. A supercell consisting of a (3 \times 1) surface unit cell was employed, and a periodic slab model containing 18 atomic layers was used to simulate the anatase TiO₂(101) surface, corresponding to 36 Ti and 72 oxygen atoms in the slab. During the structural optimizations, the outermost 9 atomic layers were allowed to relax in all the directions, whereas the other atomic layers were fixed at the bulk positions. Total energy calculations were performed by the Kohn–Sham method using the Perdew–Burke–Ernzerhof (PBE) exchange–correlation functionals, and the effects of spin polarization were considered. The kinetic cutoff energy for the plane-wave expansion was set at 400 eV and a (2 \times 2 \times 1) Monkhorst–Pack k-point mesh was used for the integration in the reciprocal space. All the calculations were carried out using the Vienna ab initio simulation package (VASP). The binding energies (BEs) can be expressed as follows:

$$\text{BEs} = E_{\text{TiO}_2(101)} + E_{\text{AEM}} - E_{\text{AEM/TiO}_2(101)}$$

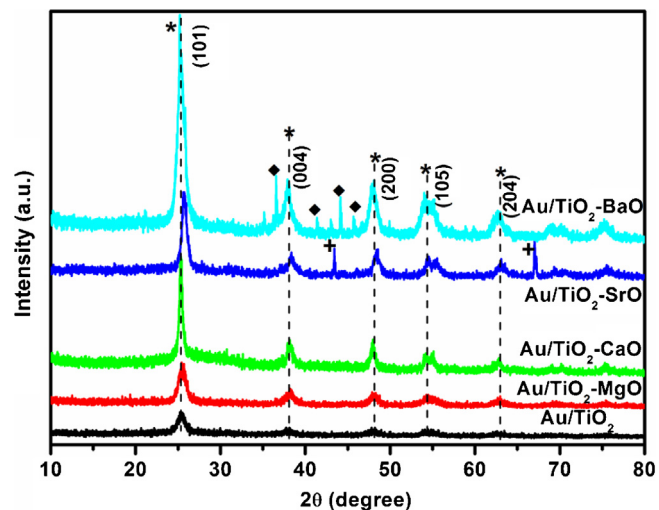


Fig. 1. XRD patterns of Au/TiO₂ and Au/TiO₂–AEMO samples. Symbols of *, ◆ and + denote anatase, BaO and SrO, respectively.

where $E_{\text{AEM/TiO}_2(101)}$, $E_{\text{TiO}_2(101)}$, and E_{AEM} represent the total energies of the adsorbed system, clean TiO₂(101) surface, and ground state of AEM atom, respectively.

3. Result and discussion

3.1. Structure and catalytic activities of Au catalysts

The XRD results of Au/TiO₂–AEMO samples (Fig. 1) show that TiO₂ is crystalline with the characteristic diffraction peaks of the anatase phase. Au/TiO₂–SrO and Au/TiO₂–BaO exhibited the diffraction peaks corresponding to SrO and BaO, however, Au/TiO₂–MgO and Au/TiO₂–CaO did not exhibit the diffraction peaks of MgO and CaO because the amounts of MgO and CaO were below the detection limit of XRD (the contents of AEMO in the four Au/TiO₂–AEMO samples follows the order: CaO < MgO < SrO < BaO). In addition, the diffraction peak of Au was not observed in all the samples because of a low content of Au or a high dispersion of Au at the supports. Compared to Au/TiO₂, the TiO₂ peaks did not change in the four Au/TiO₂–AEMO samples, indicating that AEM did not probably incorporate and substitute Ti in the TiO₂ lattices. The Raman spectra of Au/TiO₂–AEMO samples exhibited mainly the Raman bands of the anatase TiO₂ (Fig. S1, Supporting information (SI)). However, the minor blue shift of Raman bands caused by AEMO (the magnified pattern of Fig. S1) originated from the interaction between TiO₂ and AEMO. Notably, no bands were observed for AEMO due to its possible warping role in the pelletizing of titanium ethylene glycol precursor in the hydrothermal treatment. The SEM patterns of all the samples in Fig. S2 shows the microsphere structure of TiO₂ itself ($\sim 700 \text{ nm}$ in diameter), and the diameters increased with the increase in the AEMO radius. More detailed structural features on the Au NP sizes and distributions in the samples were determined from the analyses of TEM images (Fig. S3). The Au NPs with a mean diameter of $\sim 9.0 \text{ nm}$ exhibited a similar particle-size distribution in all the samples as shown in the corresponding histograms of Fig. S3, indicating that the different supports did not cause the change in the deposition and growth of Au NPs during the synthesis. Note that there also exist some small Au NPs (ca. 5 nm) in all the samples (seen in Fig. S3 (a'–e')). Moreover, as shown in the high-resolution TEM inset images of Fig. S3, Au NPs had intimate contact with both the AEMO and TiO₂. The inset of Fig. S3 indicates that AEMO was crystallized with its characteristic lattice fringes as a possible thin sheet, which was located in the edge of Au and TiO₂ by a close contact. The close contact between

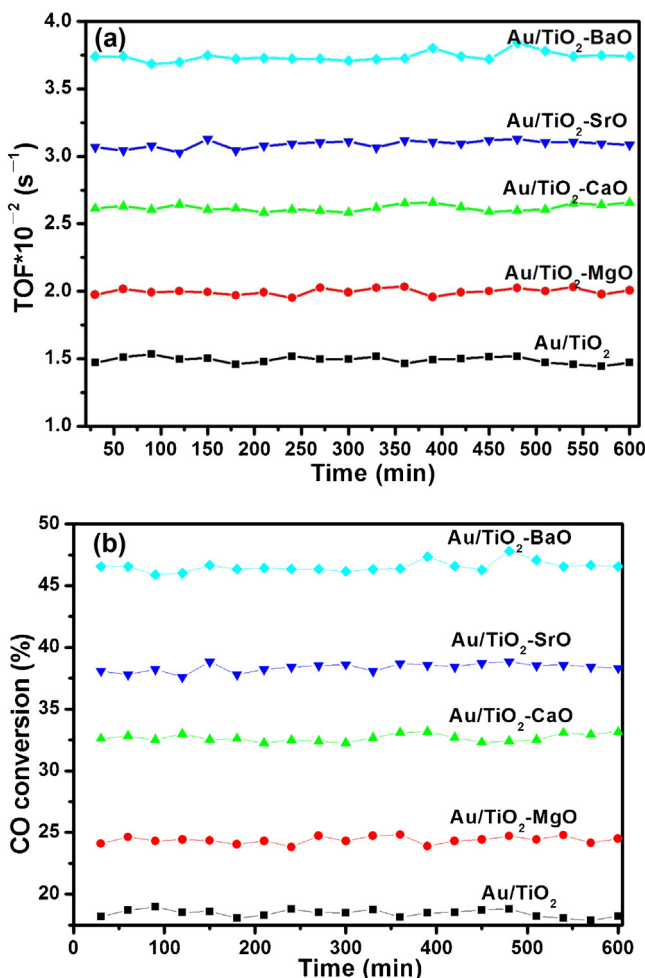


Fig. 2. The TOFs (a) and conversion (b) of CO oxidation as function of reaction time over Au/TiO₂ and Au/TiO₂-AEMO catalysts at 25 °C.

AEMO and Au may also be observed by the LSPR of Au NPs. As shown in Fig. S4, all the Au/TiO₂-AEMO samples exhibited the LSPR peak of Au NPs at $\sim 550 \text{ nm}$ [29a], but each peak had a small change at the absorption region and its intensity, which was not attributed to the effect of Au NP size (the similar Au NP size in Fig. S3), but may be caused by the sensitivity of the LSPR of Au NPs to the surrounding environment [29b] (a larger atomic radius of AEMO agrees well with a sharper absorption band and red shift in the LSPR peak of Au NPs). This interaction among Au, AEMO and TiO₂ may affect the catalytic activity of Au catalysts for CO oxidation.

Fig. 2 shows the catalytic performances of Au/TiO₂ and Au/TiO₂-AEMO samples for oxidizing CO at room temperature. The catalytic activity of each catalyst was normalized with respect to the surface Au atoms and expressed in terms of TOF (the turnover numbers of CO to CO₂ on per Au atom per second, s^{-1}). These plots of TOF and CO conversion clearly indicate that Au/TiO₂-AEMO catalysts exhibit the increasing catalytic activity with an increase in the atom radii of AEM elements (Ba > Sr > Ca > Mg). And also the normalized reaction rates of the catalysts in the Table 1 exhibit the order of the catalytic performances similar to that of TOF and CO conversion (Au/TiO₂-BaO > Au/TiO₂-SrO > Au/TiO₂-CaO > Au/TiO₂-MgO > Au/TiO₂). The catalyst based on the BaO decoration (Au/TiO₂-BaO) exhibits approximately three-fold higher TOF than Au/TiO₂ catalyst at room temperature, the highest among all the catalysts at any time period. Also, TiO₂-BaO and TiO₂ support have no catalytic

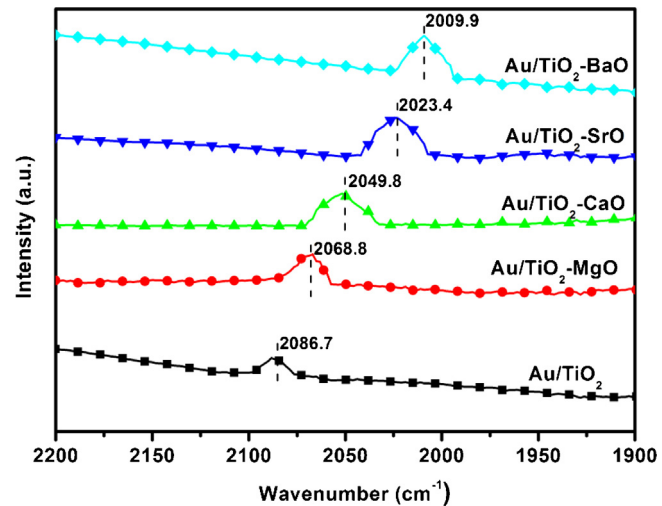


Fig. 3. FT-IR spectra of CO adsorption over Au/TiO₂ and Au/TiO₂-AEMO samples.

activity, demonstrating that the increased activities can not stem from the role of TiO₂-AEMO support.

As an another important factor, in many previous reports [30,31], the presence of small amounts of moisture and surface hydroxyls had more recently been shown to significantly affect the CO oxidation of Au/TiO₂. Therefore, the unified surface structure containing moisture is indispensable; otherwise, the contribution of the origin and nature of AEMO to the enhancement in the E_F of support may have been mistaken for the increase in the amount of surface water. During the testing of the catalytic performance of all the samples, the humidity conditions of the feed gas containing 0.3 vol% CO, 0.3 vol% O₂ and a balance of He in the same gas cylinder were identical. Considering the possible difference of surface hydroxyls in different samples, the FT-IR spectra of Au/TiO₂ and Au/TiO₂-AEMO samples without thermal treatment at $T = 293 \text{ K}$ in the transmission mode are justified in Fig. S5. No significant differences were observed at 3687.5, 3416.8 and 1628.5 cm⁻¹ (the former band was assigned to the surface hydroxyls, and the two latter bands were assigned to the adsorbed water) [30]. In other words, the addition of AEMO did not change the amount of surface hydroxyls or surface water on the catalysts. Therefore, the effect of moisture induced by AEMO over Au/TiO₂ on CO oxidation may be negligible.

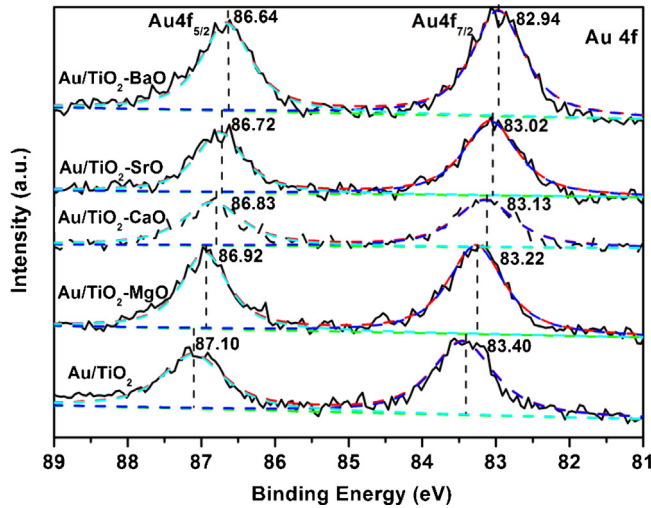
3.2. Electron transfer observation from support to Au catalysts

Considering that all the Au/TiO₂-AEMO samples have similar Au NP sizes and amount of surface hydroxyls, even though the electronic properties of Au NPs on oxide supports contribute to their catalytic activity for low-temperature CO oxidation [32], the above promoting effect of AEMO can also be attributed to a change in the charge state of Au NPs induced by AEMO. To prove this assumption, a series of experiments were carried out.

The charge state of Au NPs can be determined from the IR vibrational features of adsorbed CO at Au sites. Herein, the shift in CO stretching frequency ($\nu(\text{CO})$) is shown to be related to the surface electron densities of Au NPs, to the extent of lower frequency on electron-rich Au NPs and higher frequency on electron-deficient Au NPs [20,33]. As shown in Fig. 3, the IR band at $\sim 2086.7 \text{ cm}^{-1}$ on Au/TiO₂ was assigned to $\nu(\text{CO})$ adsorbed at metallic Au⁰ sites based on previous investigations [24–26,34,35]. The $\nu(\text{CO})$ in the presence of CO which bound to the Au sites of the Au/TiO₂-AEMO substrate shifted to a lower frequency (2068.8, 2049.8, 2023.4 and 2009.9 cm⁻¹ for Au/TiO₂-MgO, Au/TiO₂-CaO, Au/TiO₂-SrO and Au/TiO₂-BaO, respectively) compared to that of Au/TiO₂, because

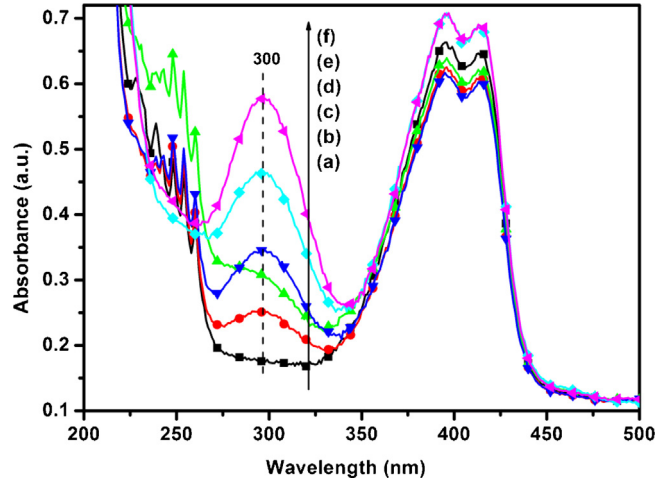
Table 1Catalytic activities of Au/TiO₂ and Au/TiO₂–AEMO catalysts for oxidizing CO at 25 °C.

Catalyst samples	Reaction rates (r_{CO}) ($\times 10^{-5}$ mol g _{Au} ⁻¹ s ⁻¹)	TOF of CO ($\times 10^{-2}$ s ⁻¹)	CO conversion (%)
Au/TiO ₂	8.99	1.50	18.50
Au/TiO ₂ –MgO	12.13	2.02	24.88
Au/TiO ₂ –CaO	15.68	2.63	32.50
Au/TiO ₂ –SrO	18.98	3.10	38.30
Au/TiO ₂ –BaO	22.59	3.75	46.50

Fig. 4. XPS spectra of Au 4f on Au/TiO₂ and Au/TiO₂–AEMO samples.

of a stronger back-donation from the Au NPs to the antibonding $2\pi^*$ orbital of CO [36]. This indicates that the introduction of AEMO to TiO₂ increased the surface electron densities of Au sites (BaO > SrO > CaO > MgO). Thus, the charge transfer from the support to the Au atoms was considered as an important factor for the enhanced catalytic activity of Au NPs, not limited to a pure reducible oxide support [37]. However, the peak intensity (a transmission spectrum signal) of CO adsorption was too weak and wide to identify the several different vibration frequencies over the same sample.

Ex-situ XPS can be used to detect the charge transfer between Au and the support surfaces [38]. Therefore, this method was employed to investigate the change in the surface states of Au NPs supported on TiO₂–AEMO by comparing the shifts of Au 4f BE. Fig. 4 shows the Au 4f spectra of Au/TiO₂ and Au/TiO₂–AEMO samples, in which the Au 4f doublet signal exhibited a symmetrical feature with the $4f_{5/2}$ and $4f_{7/2}$ centered at 87.10 and 83.40 eV, respectively, at the initial stage of AEMO-free, below the BE value of the bulk Au [24]. This is because in negatively charged Au NPs, the charge transfer occurred from TiO₂ sites to Au NPs [25,26]. The Au doublet peaks for AEMO modification shifted towards lower BE (BaO < SrO < CaO < MgO) and the Au 4f_{7/2} component reached 82.94 eV when BaO was added. Moreover, the O1s spectra in Fig. S6(a) indicate that all the samples possessed three kinds of chemical states including lattice oxygen (O_{L1}(Ti–O) and O_{L2}(AEM–O)) and chemisorbed hydroxyl oxygen (O_H) (the results of curve fitting are showed in Table S1 of SI). Based on the XPS analysis, the data of the atomic number ratio of O_{L1} to Ti and the content of relative surface oxygen vacancies (SOVs) content are shown in Table S2. The AEMO treatment decreased the atomic number ratio of O_{L1} to Ti, confirming that the composite systems were in the state of defects with SOVs. Interestingly, the Ti 2p and O1s (Fig. S6) surface features slightly shifted towards a higher BE than the AEMO-free surfaces and the Ti 2p surface features showed a symmetrical signal. Therefore, it is reasonable to speculate that AEMO can promote the

Fig. 5. UV-vis absorption spectra of TCNE solution (1 g L⁻¹) in acetonitrile. (a) TCNE without catalysts cultivating; (b)–(f): Spectra of the TCNE solution of acetonitrile after breeding the Au/TiO₂, Au/TiO₂–MgO, Au/TiO₂–CaO, Au/TiO₂–SrO and Au/TiO₂–BaO, respectively, for 30 min.

electron transfer from a support to Au NPs. Furthermore, similar to alkali metals in enhancing the redox activities of several supported metal catalysts [39,40] by weakening the bonds in diatomic molecules, the AEMO effect may originate from the alkaline earth metal mediated electron confinement and a high surface basic strength, resulting in enhanced back-donation of electrons to the reactants. This aforementioned observation can be explained by the enhanced charge transfer from the support surfaces induced by AEMO to the Au NPs, where the charge transfer is localized to Au atoms adjacent to the support sites [41]. Therefore, it is reasonable that the effect of charging on the electronic structure of Au NPs is strengthened with the increase in the atomic radius of AEMO. This experimental observation from the XPS result of the negative shift of Au BE clearly provides the direct experimental evidence for the above process.

To further investigate the behavior of AEMO over Au/TiO₂ towards CO oxidation, new strategies should be developed to detect and measure the surface electrons, where the confined electrons on the surfaces of Au/TiO₂–AEMO are transferred to the pertinent environment (electron acceptors), such as CO or O₂ adsorption. The introduction of special electron acceptors is also a method to detect the surface electrons of samples. As reported by Wang et al. [42], tetracyanoethylene (TCNE) was employed as a probe molecule with low-energy π^* orbitals to shed light on the free electrons in Au catalytic systems and the approximate threshold value of electron transfer. UV-vis spectroscopy can be used to monitor the electron-transfer reactions between Au catalysts and electron acceptors in an acetonitrile solution. Herein, the formation and change in the absorption peak at ~300 nm show that TCNE combines with electrons to generate an electron–TCNE complex (TCNE[−]). Fig. 5 shows that the fresh TCNE acetonitrile solution did not show an absorption peak at 300 nm; however, the suspension solution with Au/TiO₂ showed a weak absorption peak at 300 nm that can be assigned to TCNE[−] [42]. The increase in the peak intensity in the presence

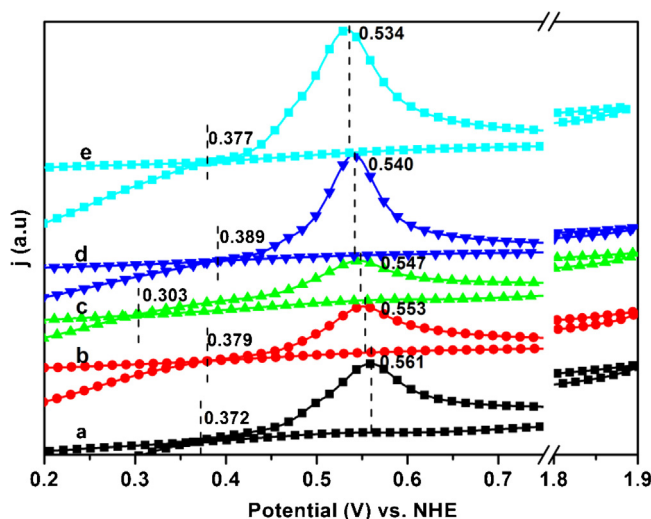


Fig. 6. CO stripping voltammograms recorded at Au/TiO₂ and Au/TiO₂–AEMO samples in CO-saturated 0.1 M HClO₄, a temperature of 298 K, scan rate = 0.02 V s⁻¹. (a) Au/TiO₂, (b) Au/TiO₂–MgO, (c) Au/TiO₂–CaO, (d) Au/TiO₂–SrO, and (e) Au/TiO₂–BaO.

of AEMO promoters (BaO > SrO > CaO > MgO) can be explained by the presence of more electrons on AEMO surfaces. The AEMO-mediated electron enrichment can be attributed to the electron transfer from TiO₂–AEMO support to Au NPs. With the introduction of AEMO, the greater absorption peaks of TCNE⁻ in Fig. 5 indicate that more electrons are transferred to the TCNE molecules by electron-transfer reactions [43]. To a certain extent, the redox couple mode (TCNE/TCNE⁻) evaluating this electron accumulation property and the ability to titrate the stored electrons can provide specific evidence for AEMO as an electron promotion on Au/TiO₂.

3.3. Electrochemical evidence of electronic interaction between support and Au in electrochemical media

The aforementioned difference in the degree of back-donating electron promotion can also be confirmed by the variation of CO oxidation in the electrochemical media indirectly. It has been reported [44] that the electronic effect of the Ti-based support may significantly increase the CO electro-oxidation compared to carbon-supported catalysts. Furthermore, a recent study [45] on the driving force of catalytic CO oxidation over Au-TiO_x, which involves the electronic interaction between Au and TiO_x instead of Au NP size effect, has been proposed by the electrochemical media experiments. In this report, it was found that the onset potential for CO oxidation on the bulk Au electrode (corresponding to the unsupported Au NPs) was around 0.7 V and a diffusion-limited current plateau was observed up to around 1.4 V, but Au NPs supported on TiO_x appeared more negative potential than the bulk Au electrode, which could be attributed to the electron transfer from TiO_x support to Au NPs [45]. Fig. 6 shows the CO stripping and the subsequent voltammograms of Au/TiO₂ and Au/TiO₂–AEMO samples in acidic media of 0.1 M HClO₄ solutions saturated with CO over the potential ranging from 0.0 V to +1.9 V (versus a reversible hydrogen electrode (RHE)). It can be observed that the voltammetric pattern in all samples showed a single, broad oxidation wave with different onset and main oxidation peak values. Herein, the onset potential on Au/TiO₂ is located in 0.372 V; however, the main oxidation peak potential with a large double-layer charging current as the potential window is located in 0.561 V. According to the above reports [45], the single symmetric peak indicates that only the oxidation of CO to CO₂ occurred during this process, while the main peak potential of CO oxidation on Au/TiO₂ (corresponding to the main oxidation peak potential) in Fig. 6 is related to the

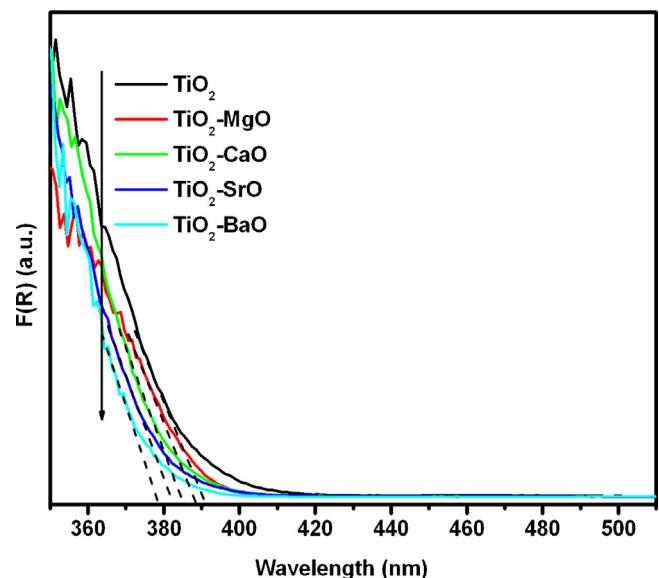


Fig. 7. UV–vis diffuse reflection spectra of TiO₂ and TiO₂–AEMO support samples.

Table 2

Onset and main oxidation peak potential values for CO electro-oxidation on Au/TiO₂ and Au/TiO₂–AEMO catalysts.

Catalyst samples	Onset peak potentials (V)	Main peak potentials (V)
Au/TiO ₂	0.372	0.561
Au/TiO ₂ –MgO	0.379	0.553
Au/TiO ₂ –CaO	0.303	0.547
Au/TiO ₂ –SrO	0.389	0.540
Au/TiO ₂ –BaO	0.377	0.534

The main oxidation peak potentials in acidic media increases in the following order: Au/TiO₂ > Au/TiO₂–MgO > Au/TiO₂–CaO > Au/TiO₂–SrO > Au/TiO₂–BaO.

charge transfer from TiO₂ to Au surfaces. The lower the main peak potential, the more the electron transfer from the support to Au [24,45]. Compared to that of Au/TiO₂, the main oxidation peak potentials of Au/TiO₂–AEMO samples decreased as follows: Au/TiO₂–BaO < Au/TiO₂–SrO < Au/TiO₂–CaO < Au/TiO₂–MgO < Au/TiO₂ (seen in Table 2), indicating that the addition of AEMO to TiO₂ can promote the electron transfer from the support to the Au surface followed by the oxidation of CO. Moreover, a more negative potential for Au/TiO₂–BaO means a stronger electron effect of BaO. However, the change in voltammetric profiles with a substantial potential intensity and the current densities for the modification of AEMO on Au/TiO₂ could not be compared. This can be attributed to the discrepancy in the peak height or current resulting from a drawback in the artifact cell design. In fact, a higher CO diffusion current can be achieved if diffusion occurs not only through the solution phase, but also through the gas phase [45]. In this case, the contribution from CO diffusion through the gas phase cannot be avoided.

During the testing of CO electro-oxidation, although the activation of water (not oxygen) in the electrochemical case provides the oxidant in the Langmuir–Hinshelwood reaction, the developed model can explain similar electron-transfer behavior described in the gas-phase CO oxidation [46]. The conclusions are clear and intriguing in which such charge interactions between AEMO-assisted support and Au are mimicked and reconfirmed by the emphasized electrochemical media. The increased electrocatalytic activities for CO oxidation induced by AEMO can be the main consequence of the electronic effect between Au and support, as also clearly indicated by the XPS, IR and TCNE/TCNE⁻ results.

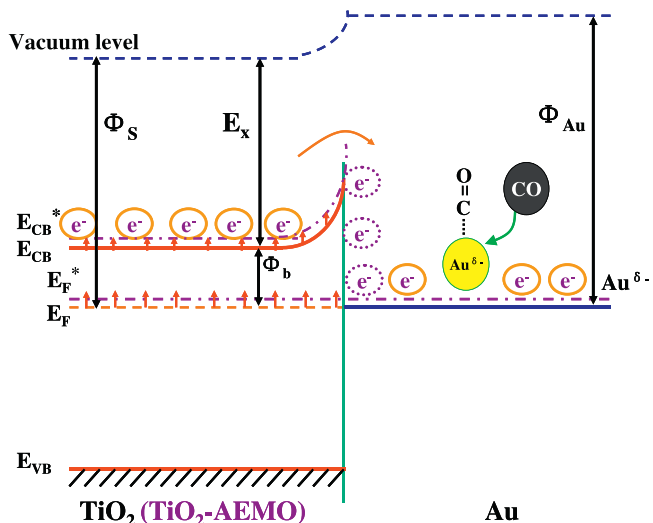
Table 3

The flat-band potential for the different supports.

Support samples	The flat-band potential (V)	Band gap (eV)
TiO ₂	−0.32	3.17
TiO ₂ –MgO	−0.33	3.19
TiO ₂ –CaO	−0.37	3.22
TiO ₂ –SrO	−0.38	3.24
TiO ₂ –BaO	−0.40	3.27

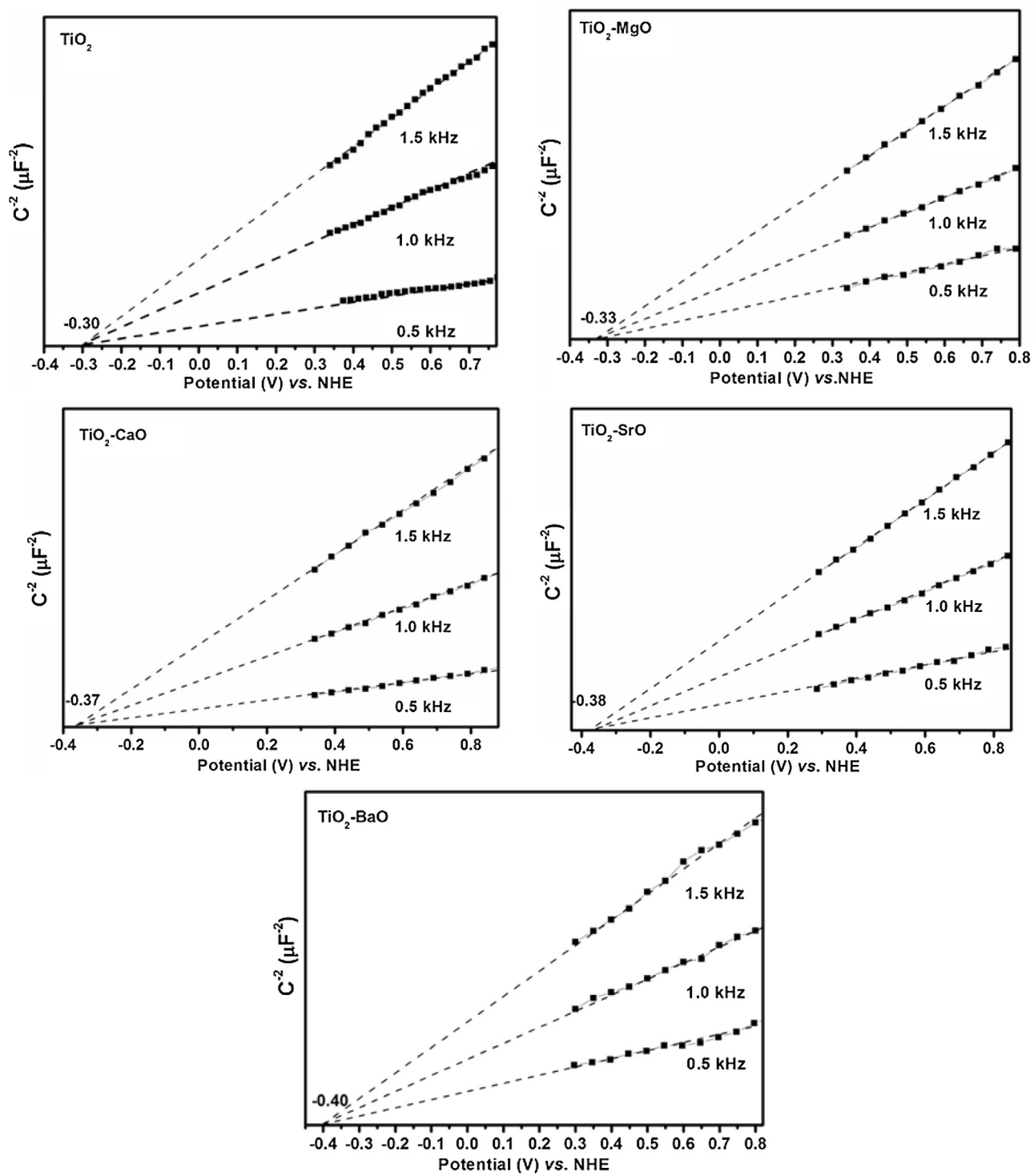
3.4. Calculation consideration for the origin of the AEMO promoters

Although the above diverse experimental methods have confirmed that AEMO-assisted support can further increase the electronic interactions and charge transfer from the support to the Au sites, the deep-rooted reason is always unclear due to that AEMO can't have the change of valence state and the ability of electron gain or loss [47,48]. Thus, to gain insight into the essence of the electron promotion, the absorption onsets and band gaps of these model supports are summarized in Fig. 7 and Table 3, exhibiting a systematic blue shift as the increase in the atomic radii of AEMOs. Correspondingly, because the conduction bands for *n*-type semiconductors are very close to their flat-band potentials [49], the measured flat-band potentials of the different supports deduced by Mott–Schottky plots in Fig. 8 and Table 3 confirm the enhancement in the E_F of AEMO-modified TiO₂, almost in agreement with increasing band gaps. Moreover, the density functional theory (DFT) calculations were carried out to investigate the configurations and electronic structures of the AEMO-modified TiO₂ surfaces. Herein, the TiO₂–AEMO composite systems were in the state of defects with SOVs (as shown in the XPS results, Table S2, of SI). Therefore, in order to keep the amounts of O atoms in the composite systems, a simplified model that assumes one alkaline earth metal (AEM, instead of AEMO) adsorbed on a (3 × 1) supercell of anatase TiO₂(101) surface was employed to qualitatively simulate the AEMO-modified TiO₂ surfaces. After exploring several possible adsorption sites on each AEM, the results indicate that the most energetically favorable binding site depends on the size of AEM atom. As displayed in Fig. 9a, for the Mg atom with a small size, the site just between two bridging oxygen (O_{2c}) atoms on the surface was obtained. Notably, in this configuration, in addition to the two O_{2c} atoms, the Mg atom was also bound to two neighboring in-plane oxygen (O_{3c}) atoms, and the lengths of Mg–O_{2c} and Mg–O_{3c} bonds are listed in Table 4. Similar configuration was also predicted for the adsorption of Ca atom. However, because of a large size, the Sr and Ba atoms prefer the site that deviates from the position between two O_{2c} atoms, and they tend to move towards one O_{3c} atom (Fig. 9b). Thus, the Sr and Ba atoms were three-fold coordinated on the anatase TiO₂(101) surface, and the lengths of the associated adsorption bonds are shown in Table 4. As the AEM changed from Mg to Ba, the calculated binding energies were 3.11, 4.52, 4.09, and 4.38 eV, respectively, indicating that the BEs did not clearly correlate with the size of AEM atoms. This nonmonotonic behavior of the BE is caused by the difference in the number of adsorption bonds. Correspondingly, if the BEs per adsorption bond are considered, a monotonical increase with the size of AEM was observed, and the corresponding values were 0.78, 1.13, 1.36, and 1.46 eV, respectively. To obtain the E_F with respect to the vacuum level, the surface work function was further determined for the most stable structure of different AEM-modified TiO₂(101) surfaces. The surface work functions of four systems are shown in Table 4, which were calculated as the deviation between the potential at the middle of the vacuum region and E_F . Interestingly, the surface work function decreased (corresponding to the elevation of E_F) monotonically when the size of AEM increased, revealing a



Scheme 1. A schematic illustration showing the possible process of electron transfer between Au and support over the well-assembled Au systems. Here, Au ($\Phi_{Au} = 5.1$ eV) has a higher work function than that of TiO₂ or TiO₂–AEMO (Φ_s , Table 3), electrons can transfer from support to Au until a dynamic equilibrium is reached and followed by generating a depletion layer (Schottky barrier Φ_b , E_x denotes the kinetic energy of electrons) at the Au/support interfaces. Adding AEMO can heighten the Fermi level of TiO₂ (from E_F to E_F^*) and its conductive band level (from E_{CB} to E_{CB}^*). Consequently, the more electrons offTiO₂–AEMO will transport across the Au/supports interface to Au, resulting in the promoted activation of CO adsorbed at Au sites. Moreover, the electron-donating ability of TiO₂–AEMO enhances with the elevation of its Fermi level in the following order: TiO₂–BaO > TiO₂–SrO > TiO₂–CaO > TiO₂–MgO.

gradual enhancement in the electron-donating ability of TiO₂(101) surface as the AEM changed from Mg to Ba. This result implies that the charge transfer from AEM-modified TiO₂(101) surface to the Au NPs became easier in the same sequence. Moreover, according to the calculated band structures (see Fig. S7 in the SI), the band gaps of AEM-modified TiO₂(101) surfaces were obtained, and the values are summarized in Table 4. It is well known that the pure DFT method usually underestimates the band gap of semiconductors due to insufficient cancellation of the self-interaction correction inherent in the local exchange functionals. As expected, the calculated band gaps are smaller than the measured values (Table 3). However, both theoretical and experimental results indicate that the band gap of AEM-modified surface increased slightly as the size of AEM increased. Therefore, the theoretical calculations also demonstrate that the E_F and band gap of the anatase TiO₂(101) surface can be improved by depositing AEM atoms, thus increasing the electron transfer from the modified supports to the Au sites. The higher E_F of TiO₂–AEMO supports shows the existence of a stronger electron transfer from the support to the Au. Therefore, the AEMO-assisted effect allows the modification and control of the electronic structure of TiO₂ in activating the Au NPs by charge transfer. As a result, the Au NPs with high electron densities suitably adjusts the chemical reactivity. In addition, according to the density of states of AEM atom (see Fig. S8 in the SI), the surface states dominated by the contributions of AEM did not appear in the band gap of TiO₂(101) substrate. Considering the above fact, a possible schematic diagram of electron-transfer processes by forming an ideal Schottky barrier between Au and supports over the well-assembled Au systems is also displayed in Scheme 1. Therefore, the Mott–Schottky and calculation results indicate that the promoting effect of AEMO on Au/TiO₂ for oxidizing CO is closely related to the elevation of E_F in TiO₂ (i.e., the decrease in surface work function) induced by AEMO, which may be beneficial to understand the origin of promoters.

Fig. 8. Mott-Schottky plots for TiO_2 and TiO_2 -AEMO support samples.**Table 4**

The calculated binding energy, the average lengths of different adsorption bonds, the surface work function, and the band gap for the most stable structure of AEM adsorbed on anatase $\text{TiO}_2(101)$ surface.

	$\text{Mg}/\text{TiO}_2(101)$	$\text{Ca}/\text{TiO}_2(101)$	$\text{Sr}/\text{TiO}_2(101)$	$\text{Ba}/\text{TiO}_2(101)$
Binding energy (eV)	3.11	4.52	4.09	4.38
Band gap (eV)	1.73	1.75	1.76	1.77
$d(\text{M}-\text{O}_{2c})$ (Å)	$1.917(\times 2)$	$2.163(\times 2)$	$2.290(\times 2)$	$2.425(\times 2)$
$d(\text{M}-\text{O}_{3c})$ (Å)	2.027, 2.131	2.314, 2.406	2.494	2.683
Surface work function (eV)	4.53	4.14	3.91	3.75

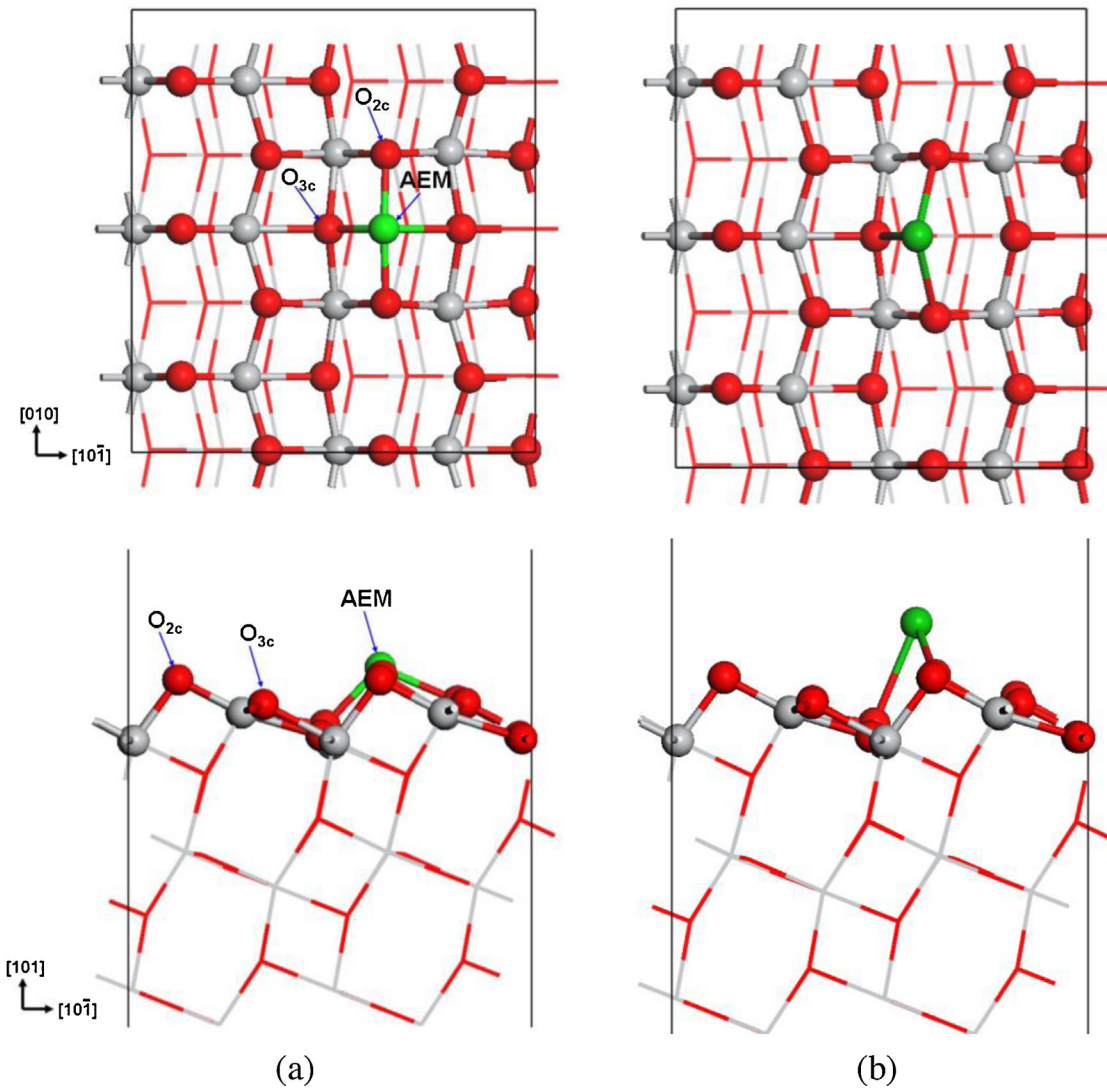


Fig. 9. The top (upper panel) and side views (bottom panel) of the most stable configuration for the adsorption of (a) Mg (Ca) and (b) Ba (Sr) atom on the anatase TiO_2 (101) surface. The Ti, O, and AEM atoms are denoted by gray, red, and green spheres, respectively, and only part of TiO_2 (101) surface is displayed in the side view. For interpretation of the references to color in this figure legend, the reader is referred to the web version of this article.

4. Conclusions

In summary, the TiO_2 –AEMO supported Au catalysts exhibited a higher catalytic activity for oxidizing CO at room temperature than TiO_2 -supported Au catalyst, which may be attributed to the electron promotion of AEMO for increasing the E_F of support and then increasing the surface electron densities of Au sites from the results presented above. The support-dependent and electron-transfer activity based on the AEMO modification here establish an instance to consider the origin of the enhanced activity of supported Au NPs towards CO oxidation in a different view. The AEMO-modified TiO_2 supports significantly affected the Au-support interactions by changing the surface electronic properties of the support. To bridge this gap, a series of methods were developed to understand the higher electron densities of Au NPs and higher electron transfer to the surrounding environment for Au/TiO_2 –AEMO samples. The XPS and IR results of CO adsorption revealed the significant enhancement in the surface electron densities of Au NPs induced by AEMO. The redox couple mode (TCNE/TCNE[–]) testing showed that AEMO modification could promote the transfer of confined electrons on Au catalysts to the pertinent environment. In addition, the AEMO-modified Au catalysts (Au/TiO_2 –AEMO) can cause a more negative

main oxidation potential for CO electrochemical oxidation compared to the AEMO-free Au catalyst (Au/TiO_2). The promoting effect of AEMO reflects that although earlier general studies highlighted the findings of structural promotion in the sintering resistance of Au NPs for CO oxidation, the new adopted characterizations from this study provided a different insight into the predominant electronically promoted effects of AEMO. These findings in conjunction with DFT calculations have also disclosed that the AEMO-modified supports demonstrate the aforementioned remarkable chemical activation of TiO_2 in E_F to enable subtle features in the electronic structure of the catalysts (the higher the E_F of the support, the higher the activity of the catalyst). This may also establish a theoretical guide (by adjusting the E_F of semiconductor support) in designing or modifying thermo-catalysts.

Acknowledgments

This work was financially supported by the National Natural Science Foundation of China (nos. 21273037, 21373048, and 21203027), the National Basic Research Program of China (973 Program, no. 2014CB239303), the Science & Technology Plan Project of Fujian Province (no.2014Y2003), and the Independent Research

Project of State Key Laboratory of Photocatalysis on Energy and Environment (2014A02) of China.

Appendix A. Supplementary data

Supplementary data associated with this article can be found, in the online version, at <http://dx.doi.org/10.1016/j.apcatb.2015.10.046>.

References

- [1] O.H. Laguna, A. Pérez, M.A. Centeno, J.A. Odriozola, *Appl. Catal. B* 176 (2015) 385–395.
- [2] M. Date, M. Okumura, S. Tsubota, M. Haruta, *Angew. Chem. Int. Ed.* 43 (2004) 2129–2132.
- [3] G.C. Bond, D.T. Thompson, *Catal. Rev. Sci. Eng.* 41 (1999) 319–388.
- [4] C. Qi, S. Zhu, H. Su, H. Lin, R. Guan, *Appl. Catal. B* 138 (2013) 104–112.
- [5] M.S. Chen, D.W. Goodman, *Science* 306 (2004) 252–255.
- [6] D. Matthey, J.G. Wang, S. Wendt, J. Matthiesen, R. Schaub, E. Laegsgaard, B. Hammer, F. Besenbacher, *Science* 315 (2007) 1692–1696.
- [7] B. Solsona, M. Conte, Y. Cong, A. Carley, G. Hutchings, *Chem. Commun.* (2005) 2351–2353.
- [8] J.A. Moma, M.S. Scurrell, W.A. Jordaan, *Top. Catal.* 44 (2007) 167–172.
- [9] P. Mohapatra, J. Moma, K.M. Parida, W.A. Jordaan, M.S. Scurrell, *Chem. Commun.* 10 (200) (2015) 1044–1046.
- [10] W. Yan, S.M. Mahurin, Z. Pan, S.H. Overbury, S. Dai, *J. Am. Chem. Soc.* 127 (2005) 10480–10481.
- [11] Y.F. Yang, P. Sangeetha, Y.W. Chen, *Ind. Eng. Chem. Res.* 48 (2009) 10402–10407.
- [12] Y.W. Chen, H.J. Chen, D.S. Lee, *J. Mol. Catal. A* 363/364 (2012) 470–480.
- [13] S. Li, H. Zhu, Z. Qin, G. Wang, Y. Zhang, Z. Wu, Z. Li, G. Chen, W. Dong, Z. Wu, L. Zheng, J. Zhang, T. Hu, J. Wang, *Appl. Catal. B* 144 (2014) 498–506.
- [14] A.C. Gluhoi, X. Tang, P. Marginean, B.E. Nieuwenhuys, *Top. Catal.* 39 (2006) 101–110.
- [15] L.H. Chang, Y.W. Chen, N. Sasirekha, *Ind. Eng. Chem. Res.* 47 (2008) 4098–4105.
- [16] L.M. Molina, B. Hammer, *Phys. Rev. Lett.* 90 (2003) 206102.
- [17] R.J.H. Grisel, B.E. Nieuwenhuys, *J. Catal.* 199 (2001) 48–59.
- [18] Z.P. Liu, S.J. Jenkins, D.A. King, *Phys. Rev. Lett.* 93 (2004) 156102.
- [19] A.C. Gluhoi, B.E. Nieuwenhuys, *Catal. Today* 122 (2007) 226–232.
- [20] B. Yoon, H. Hakkinnen, U. Landman, A.S. Worz, J.M. Antonietti, S. Abbet, K. Judai, U. Heiz, *Science* 307 (2005) 403–407.
- [21] A. Boffa, C. Lin, A.T. Bell, G.A. Somorjai, *J. Catal.* 149 (1994) 149–158.
- [22] S.J. Tauster, S.C. Fung, R.L. Garten, *J. Am. Chem. Soc.* 100 (1978) 170–175.
- [23] G.M. Schwab, *Angew. Chem. Int. Ed.* 6 (1967) 375–376.
- [24] K. Yang, J.F. Liu, R.R. Si, X. Chen, W.X. Dai, X.Z. Fu, *J. Catal.* 317 (2014) 229–239.
- [25] K. Yang, K. Huang, Z.J. He, X. Chen, X.Z. Fu, W.X. Dai, *Appl. Catal. B* 158/159 (2014) 250–257.
- [26] K. Yang, Y.X. Li, K. Huang, X. Chen, X.Z. Fu, W.X. Dai, *Int. J. Hydrogen Energy* 39 (2014) 18312–18325.
- [27] V. Subramanian, E.E. Wolf, P.V. Kamat, *J. Am. Chem. Soc.* 126 (2004) 4943–4950.
- [28] H. Lin, L. Ding, Z. Pei, Y. Zhou, J. Long, W. Deng, X. Wang, *Appl. Catal. B* 160/161 (2014) 98–105.
- [29] (a) L. Wu, F. Li, Y. Xu, J.W. Zhang, D. Zhang, G. Li, H. Li, *Appl. Catal. B* 164 (2015) 217–224;
(b) X.M. Feng, G. Yang, Q. Xu, W.H. Hou, J.P. Zhu, *Macromol. Rapid Commun.* 27 (2006) 31–36.
- [30] J.A. Singh, S.H. Overbury, N.J. Dudney, M.J. Li, G.M. Veith, *ACS Catal.* 2 (2012) 1138–1146.
- [31] R.R. Si, J.F. Liu, K. Yang, X. Chen, W.X. Dai, X.Z. Fu, *J. Catal.* 311 (2014) 71–79.
- [32] J.A. Rodriguez, G. Liu, T. Jirsak, J. Hrbek, Z.P. Chang, J. Dvorak, A. Maiti, *J. Am. Chem. Soc.* 124 (2002) 5242–5250.
- [33] M.S. Chen, Y. Cai, Z. Yan, D.W. Goodman, *J. Am. Chem. Soc.* 128 (2006) 6341–6346.
- [34] I.X. Green, W. Tang, M. Neurock, J.T. Yates Jr., *Science* 333 (2011) 736–739.
- [35] S. Garrettin, P. Concepcion, A. Corma, J.M. Lopez Nieto, V.F. Puntes, *Angew. Chem. Int. Ed.* 43 (2004) 2538–2540.
- [36] H. Hakkinnen, S. Abbet, A. Sanchez, U. Heiz, U. Landman, *Angew. Chem. Int. Ed.* 42 (2003) 1297–1300.
- [37] Q. Fu, H. Saltsburg, M. Flytzani-Stephanopoulos, *Science* 301 (2003) 935–938.
- [38] Z. Jiang, W. Zhang, L. Jin, X. Yang, F. Xu, J. Zhu, W. Huang, *J. Phys. Chem. C* 111 (2007) 12434–12439.
- [39] C.G. Vayenas, S. Bebelis, C. Pliangos, S. Brosda, D. Tsiplakides, *Electrochemical Activation of Catalysis: Promotion, Electrocatalytic Promotion and Metal-support Interactions*, Kluwer Academic/Plenum Publishers, New York, 2001, pp. p35.
- [40] S.J. Ahlers, M.M. Pohl, J. Radnik, D. Linke, E.V. Kondratenko, *Appl. Catal. B* 176–177 (2015) 570–577.
- [41] L. Giordano, J. Goniakowski, G. Pacchioni, *Phys. Rev. B* 64 (2001) 075417.
- [42] F. Wang, W. Ueda, J. Xu, *Angew. Chem. Int. Ed.* 51 (2012) 3883–3887.
- [43] S. Sugunan, G.D. Rani, K.B. Sherly, *React. Kinet. Catal. Lett.* 43 (1991) 375–380.
- [44] M. Roca-Ayats, G. García, J.L. Galante, M.A. Pena, M.V. Martínez-Huerta, *J. Phys. Chem. C* 117 (2013) 20769–20777.
- [45] P. Rodriguez, D. Plana, D.J. Fermin, M.T.M. Koper, *J. Catal.* 311 (2014) 182–189.
- [46] B.E. Hayden, D. Pletcher, J.P. Suchsland, *Angew. Chem. Int. Ed.* 46 (2007) 3530–3532.
- [47] M. Konsolakis, I.V. Yentekakis, *J. Catal.* 198 (2001) 142–150.
- [48] L. Xue, H. He, C. Liu, C.B. Zhang, B. Zhang, *Environ. Sci. Technol.* 43 (2009) 890–895.
- [49] A. Ishikawa, T. Takata, J.N. Kondo, M. Hara, H. Kobayashi, K. Domen, *J. Am. Chem. Soc.* 124 (2002) 13547–13553.